BRISC: Annotated Dataset for Brain Tumor Segmentation and Classification

Amirreza Fateh[a] · Yasin Rezvani[b] · Sara Moayedi[b] · Sadjad Rezvani[b] ·
Fatemeh Fateh[c] · Mansoor Fateh[b,*] · Vahid Abolghasemi[d,*]

Abstract Accurate segmentation and classification of brain tumors from Magnetic Resonance Imaging (MRI) remain key challenges in medical image analysis, primarily due to the lack of high-quality, balanced, and diverse datasets with expert annotations. In this work, we address this gap by introducing BRISC, a dataset designed for brain tumor segmentation and classification tasks, featuring high-resolution segmentation masks. The dataset comprises 6,000 contrast-enhanced T1-weighted MRI scans, which were collated from multiple public datasets that lacked segmentation labels. Our primary contribution is the subsequent expert annotation of these images, performed by certified radiologists and physicians. It includes three major tumor types, namely glioma, meningioma, and pituitary, as well as non-tumorous cases. Each sample includes high-resolution labels and is categorized across axial, sagittal, and coronal imaging planes to facilitate robust model development and cross-view generalization. To demonstrate the utility of the dataset, we provide benchmark results for both tasks using standard deep learning models. The BRISC dataset is made publicly available. datasetlink: Kaggle, Figshare, Zenodo

[a]School of Computer Engineering, Iran University of Science and Technology (IUST), Tehran, Iran
[b]Faculty of Computer Engineering, Shahrood University of Technology, Shahrood, Iran
[c]Northern Care Alliance NHS Foundation Trust (NCA), Manchester, UK
[d]School of Computer Science and Electronic Engineering, University ofEssex, Colchester, UK
E-mail: amirreza_fateh@comp.iust.ac.ir
E-mail: yasinrezvani@shahroodut.ac.ir
E-mail: sara_moayedi@shahroodut.ac.ir
E-mail: sadjadrezvani@shahroodut.ac.ir
E-mail: fatemeh.fateh@nca.nhs.uk
E-mail: mansoor_fateh@shahroodut.ac.ir
E-mail: v.abolghasemi@essex.ac.uk
*Corresponding author

Background & Summary

Brain tumors are among the most critical medical conditions, requiring accurate and timely diagnosis for effective treatment and management [1,2]. Magnetic Resonance Imaging (MRI) plays a critical tool in diagnosing and monitoring brain tumors, owing to its non-invasive imaging capabilities and ability to provide detailed visualization of brain structures [3,4,5]. Despite significant advancements in medical imaging technologies, developing automated systems for tumor detection and segmentation remains a major challenge [6,7,8]. This challenge arises primarily from the scarcity of high-quality labeled datasets designed for these tasks. Additionally, the complexity and variability of tumor appearances across patients further complicate accurate segmentation and classification [9,10,11].

Existing brain tumor segmentation datasets, such as the Brain Tumor Segmentation (BraTS) [12], Cheng [13] brain tumor dataset, and others, have significantly advanced the development of automated segmentation models. However, several limitations in these datasets drive the need for novel datasets to address emerging challenges in the field. For example, the BraTS dataset is widely used and comprehensive. However, it depends on pre-processed, standardized data that may not reflect the real-world variability in MRI acquisition protocols across institutions. Additionally, BraTS primarily focuses on gliomas and lacks representation of other tumor types, potentially limiting the generalizability of models trained on it [14,15]. The Cheng [13] brain tumor dataset, on the other hand, suffers from class imbalance and limited diversity in imaging conditions and patient demographics, which can restrict model robustness [16]. Many publicly available datasets face issues with inconsistent labeling. These inconsis-

tencies can negatively affect the training and evaluation of segmentation models [17,18,19,20]. These limitations underscore the necessity of introducing a new dataset that offers balanced class distributions, multi-institutional diversity, and high-quality expert annotations to enhance the reliability and generalizability of automated brain tumor segmentation models. Additionally, including class labels for classification tasks, such as identifying glioma, meningioma, pituitary, and non-tumorous cases, enhances the dataset's utility and supports broader real-world applications in brain tumor analysis.

To address these gaps, we present the BRISC dataset: a large-scale, balanced, and expert-annotated MRI dataset designed for both segmentation and classification of brain tumors. BRISC includes 6,000 contrast-enhanced T1-weighted MRI scans across four categories—glioma, meningioma, pituitary, and non-tumorous cases—covering multiple anatomical planes (axial, coronal, sagittal). The dataset emphasizes consistent quality, balanced distributions, and multi-institutional diversity, making it suitable for developing models that generalize across clinical settings. To demonstrate its utility, we also propose a transformer-based model, Swin-HAFNet, which integrates hierarchical attention fusion and contextual bottleneck enhancements to achieve strong performance in both segmentation and classification tasks.

Overview of Brain Tumors

Brain tumours are amongst the most fatal of all cancers [21]. Amongst paediatric solid tumours, brain tumours are most fatal and commonly occurring [21]. There is diversity in the types of brain tumours, including but not limited to gliomas which account for 45% of brain tumours with pituitary tumours and meningiomas accounting for 15% each [22]. The gold standard imaging for diagnosis of a brain tumours or brain metastases is an MRI scan with gadolinium [23]. When possible, management is initially via surgery to remove the lesion which is then sent for histological and molecular genotype identification [23]. Pre, intra and post-operative MRIs can be used to guide surgical resection and management [23,24,25]. Intra-operatively, functional MRIs visualise cerebrovascular activity which can be correlated with neuronal activity, aiding the surgical team. Other techniques such as cord simulation can also be used [24]. In many scenarios, regardless of skill, neurosurgical reach has to be limited for safety due to the presence of many functionally important regions within the organ [21,23]. Further management includes the use of medical interventions for symptomatic management, radiotherapy and chemotherapy [21]. The blood brain barrier poses challenges to medical interventions and chemotherapy, this barrier filters material entering the brain via circulation, limiting medical access to the brain [21]. Localisation of the lesion and adjacent structures via MRIs can guide both surgical and radiotherapeutic planning [26]. In summary, MRI scans are used in the initial diagnosis and management planning of brain tumours, including pre-surgical use and as guidance for radiotherapy [26].

Glioma

Gliomas are primary brain tumours, they are the most common of malignant primary brain tumours in adults [23]. They arise from glial cells or stem cells which develop glial properties during neoplastic changes [27]. Glial cells designate a group of different cells which provide support for neurons, for example by the formation of axonal myelin sheaths [28]. For adults, the most aggressive form of gliomas, the glioblastoma, has a two-year survival time [21]. Gliomas can be classified according to the WHO 2016 classification of Central Nervous System (CNS) tumours [27].

Diffuse forms of gliomas can grow in irregular shapes, extensively infiltrating brain parenchyma [27], this makes neurosurgical management difficult as safe maintenance of functional brain tissue is required during resection [21,23].

Meningioma

Meningiomas in adults are the most common, being 30% of central nervous system tumours, whilst they are rare amongst children [29]. They arise from cells on the outer layer of the arachnoid mater, a part of the meninges [29]. The meninges is a layer in the central nervous system which encompasses the brain, cerebrospinal fluid and spinal cord [30]. Though, a meningioma could arise anywhere on the meninges, 98% of meningiomas are intracranial [29]. Usually benign lesions, they can be slow growing [29]. MRI scans in conjunction with CT scan can be sued for diagnosis and treatment planning [29]. Treatment generally consists of neurosurgical treatment, occasionally in adjunct with radiotherapy [29]. Benign meningiomas can grow to a large size with pressures on the brain causing symptoms [31]. Non-benign meningiomas are associated with irregular shapes and tumours heterogeneity and therefore, benign meningiomas tend to be associated with regular shapes and homogeneity [32].

Pituitary Tumors

These are tumours originating in the pituitary gland, a small structure at the base of the brain, above the sphenoid bone [33]. The pituitary gland has an essential role in growth, metabolism and reproduction [34]. Due to this, pituitary tumours can cause a wide range of symptoms including but not limited to; mood disorders, diabetes mellitus, obesity, infertility and visual disturbances [34]. However, only one third of these tumours are symptomatic [34]. The majority of pituitary tumours are benign and when treated, treatment generally includes neurosurgical resection and radiotherapy [35].

Non-Tumorous Conditions

Non-tumorous conditions in this dataset include both normal brain scans (from subjects without visible abnormalities) and scans with non-neoplastic lesions that can mimic tumorous appearance but are not neoplastic in origin. These may represent inflammatory or vascular pathologies such as abscesses, cysts, haematomas, or aneurysms [36]. The inclusion of such cases provides a broader spectrum of appearances encountered in clinical neuroimaging and enables models to better distinguish tumorous from non-tumorous abnormalities. Due to the high soft-tissue sensitivity of MRI, these conditions can often be characterised radiologically, although histopathological confirmation (e.g., via biopsy) may still be required in practice [37].

Magnetic resonance imaging of human brain

Anatomical planes

The main anatomical planes are coronal, transverse and sagittal planes [38]. These may be more simply described as a 'front to back' vertical plane, a 'top to bottom' horizontal plane, a longitudinal 'side to side' plane [38]. For a radiologist reporting an MRI scan, the above planes are available for viewing [39].

Challenges in Brain Tumor Diagnosis

Misdiagnosis Risks

As mentioned above, some tumours do not cause symptoms until reaching a certain growth [31], this may lead to late clinical suspicion to warrant imaging. When available and possible, the best imaging modality are MRI scans [23]. Even the use of neurological imaging can lead to misdiagnosis as neoplastic and non neoplastic conditions can mimic each other. As mentioned above, there are non tumorous space occupying lesions, these can be benign, meaning surgical resection and biopsy exposes many patients unnecessarily to the risks of surgery [40]. There are also neoplastic brain lesions which do not appear as a space occupying lesion [40]. Not neglecting T1 precontrast imaging can aid avoidance of misdiagnosis [40]. Further MR imaging modalities and a thorough clinical assessment alongside some further investigations can aid in reducing errors [40]. There are certain tumours which are difficult to visualised on MRI, though MRIs provide a high level of diagnostic accuracy for most tumours [41].

Methods

The BRain tumor Image Segmentation and Classification (BRISC) dataset has been meticulously curated to address key challenges in brain tumor research, particularly in the domains of segmentation and classification tasks. It provides a balanced, high-quality collection of MRI data, annotated for both research and clinical applications. The dataset includes images with labels for four categories: Glioma, Meningioma, Pituitary tumors, and non-tumorous. By focusing on comprehensive data collection and rigorous annotation processes, the dataset aims to advance the development of robust machine learning models in medical imaging.

Purpose and Objectives

The primary goal of collecting and releasing this dataset is to overcome limitations observed in existing brain tumor datasets, such as class imbalance, lack of diversity, and annotation inconsistencies. While datasets like BraTS have driven significant advancements in glioma segmentation, their exclusive focus on gliomas and reliance on pre-processed data limit their generalizability to other tumor types and real-world scenarios. Our dataset expands the scope by incorporating multiple tumor types and includes a "non-tumorous" class to aid in broader diagnostic tasks. This addition makes the dataset highly versatile, enabling its use in applications ranging from multi-class tumor classification to binary tumor detection. The key objectives include:

1. Supporting segmentation tasks by providing accurate tumor masks.
2. Facilitating multi-class classification through balanced representation of tumor types.

Table 1: Class distribution in the training and testing parts of BRISC

Class	Training Images	Testing Images	Total Images
Glioma	1,147	254	1,401
Meningioma	1,329	306	1,635
Pituitary	1,457	300	1,757
non-tumorous	1,067	140	1,207
Total	**5,000**	**1,000**	**6,000**

Table 2: Class distribution based on MRI planes in the training and testing parts of BRISC

Class\Plane	**Train**			**Test**		
	Axial	Coronal	Sagittal	Axial	Coronal	Sagittal
Glioma	347	428	372	85	81	88
Meningioma	423	426	480	134	89	83
Pituitary	428	496	533	116	98	86
non-tumorous	352	310	405	52	48	40
Total per plane	1550	1660	1790	387	316	297
Total	**5000**			**1000**		

Dataset Composition and Planar Distributions

The dataset comprises 6,000 MRI images, divided into training and testing sets, as detailed in Table 1. This structured division ensures robust evaluation metrics while providing ample data for training advanced machine learning models. For the training dataset, the total number of images across the planes is 5,000, and for testing, the total is 1,000.

In addition to the class-based distribution, we provide another form of distribution, which is dataset composition by MRI planes. This breakdown categorizes images into Coronal, Sagittal, and Axial planes, helping to analyze how different orientations are represented in the dataset. As shown in Table 2, the distribution of different MRI planes is nearly uniform, similar to the distribution of different classes in Table 1. This balanced distribution ensures that no particular class or plane is overrepresented, which is crucial for preventing model bias and improving generalization.

Data Preprocessing

The original collection contains 7,023 brain MR images across four classes: glioma, meningioma, pituitary tumour, and non-tumorous (the latter sourced from Br35H). We then applied the following steps to ensure consistency and quality:
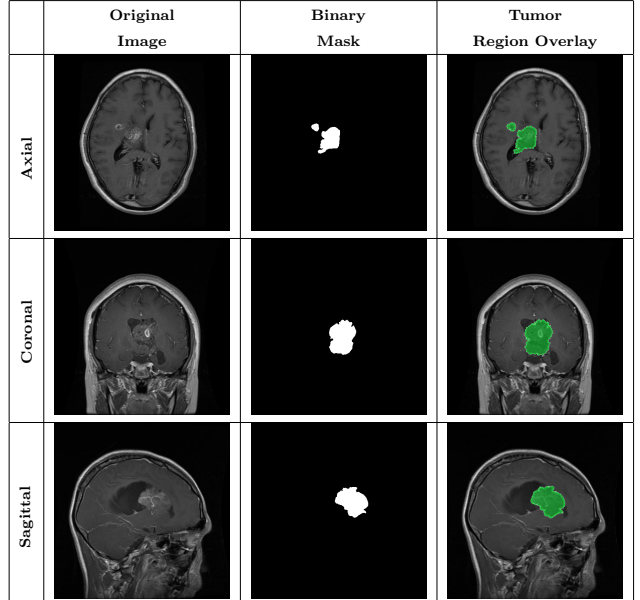

Fig. 1: Samples of Glioma segmentation across different imaging planes

- **Sequence harmonization**: Only T1-weighted MRI sequences were retained to ensure consistency.
- **Label and mask verification**: A radiologist and a physician reviewed images to identify incorrect or inconsistent labels; images with tumour la-
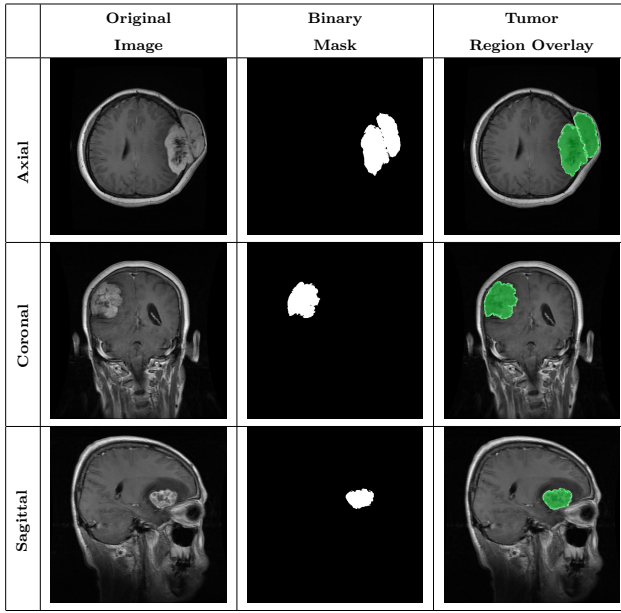
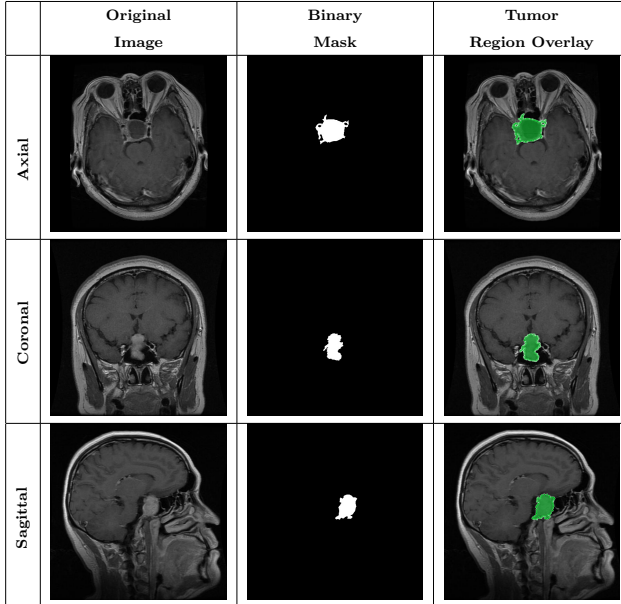Fig. 2: Samples of Meningioma segmentation across different imaging planes

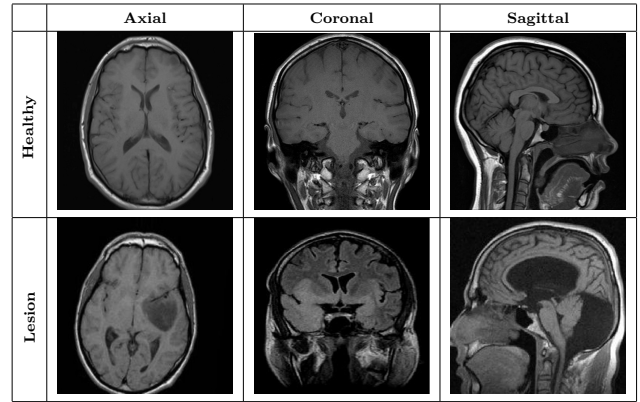Fig. 3: Samples of Pituitary segmentation across different imaging planes

Fig. 4: Samples from the non-tumorous class across different imaging planes. The top row shows healthy brain scans without visible abnormalities, and the bottom row shows examples of non-tumorous lesions (e.g., cysts or abscesses).

Fig. 5: Samples of whole-region misannotations. The red area indicates regions that were initially marked as tumors but were identified by radiologist and physician as non-tumorous.

bels unsupported by the visible image, or with empty/misaligned masks, were removed.

- **Artefact/corruption screening**: Corrupted files and images with severe artefacts were excluded.
- **De-duplication and redundancy control**: Exact duplicates and near-duplicates (including consecutive images from very short series) were removed; de-duplication was completed before any train/test split to avoid leakage and over-representation.
- **Standardization**: Images were resized and borders/margins adjusted for consistent spatial dimensions.
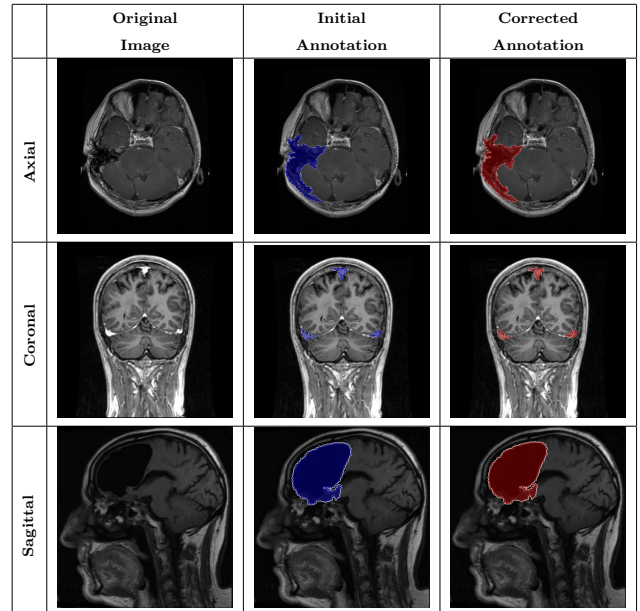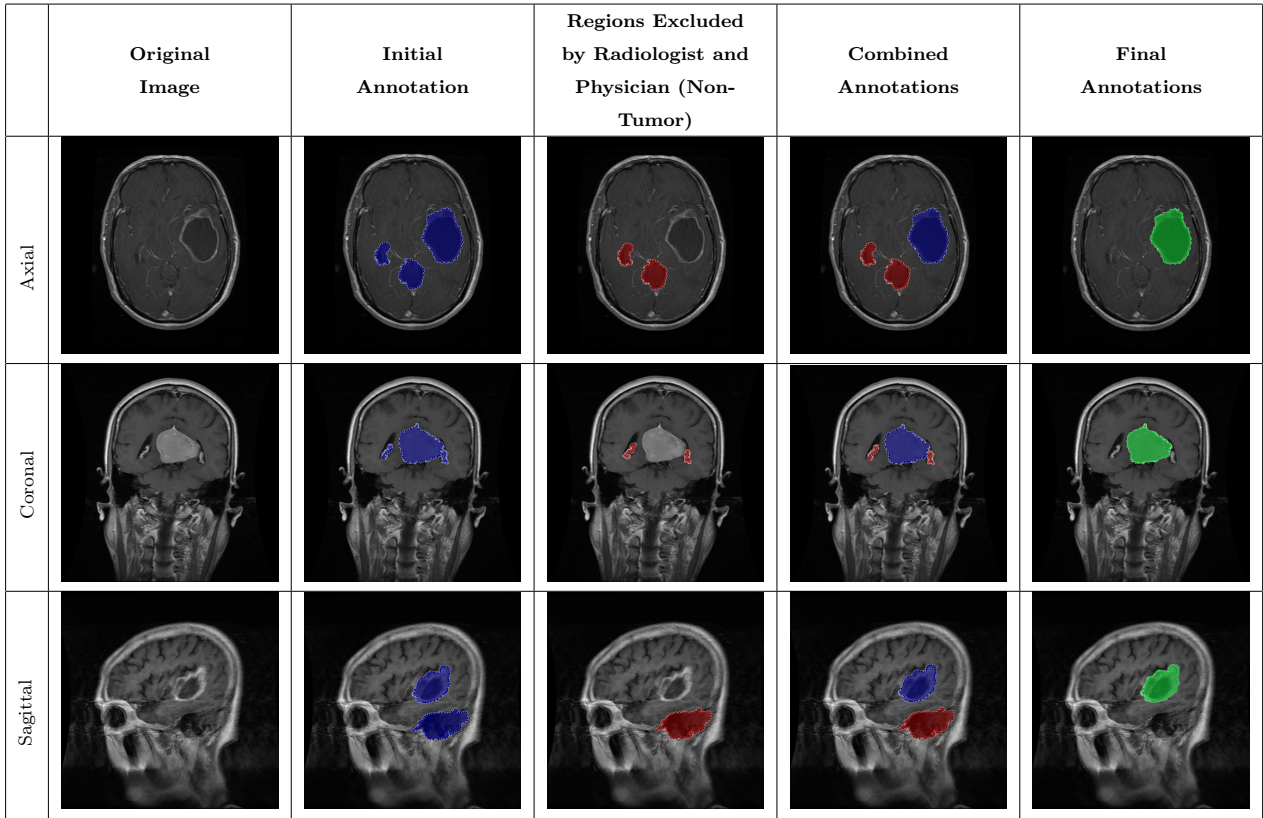
Fig. 6: Samples of partial-region overannotations. The red area indicates regions that were initially marked as tumorous but were later identified by the radiologist and physician as non-tumorous.

Imaging Details

All images in the dataset are T1-weighted contrast-enhanced MRI scans, selected specifically from the "Brain Tumor MRI Dataset" (Kaggle) [42]. Although the original dataset included some T2-weighted images, we exclusively selected T1-weighted scans for their superior ability to highlight tumor boundaries effectively. Another notable characteristic of this dataset is the length of MRI sequences. While typical brain MRI studies often consist of longer sequences, the majority of sequences in this dataset were notably short, ranging from 1 to 5 images per sequence. Sequences with only one image were excluded, as even experienced radiologists and physicians found it challenging to identify tumors accurately in these cases.

The original dataset provided only a train/test split and did not include any information about patients, sequences, or slices, making it impossible to definitively link images to the same subject. To minimize the risk of the same person appearing in both train and test sets, our annotators manually reviewed images as much as possible—through visual similarity checks and metadata cross-referencing—to separate likely same-subject cases. While complete subject-level independence cannot be guaranteed due to the source limitations, this conservative approach ensures no obvious same-patient images cross splits; multiple images from the same subject may therefore be present within a single split. This is documented in the repository metadata.

Annotation Process

The dataset underwent a meticulous annotation and review process to ensure accuracy and reliability. Annotation was performed using the AnyLabeling tool [43], which facilitated precise delineation of tumorous and non-tumorous regions. Each image was reviewed and refined multiple times with input from a certified physician and radiologist. Key steps in the annotation process included:

- **Tumor Mask Refinement**: Using AnyLabeling [43], regions corresponding to tumorous lesions were iteratively refined to ensure accurate segmentation masks.
- **Class Verification**: The "non-tumorous" class was reviewed in detail. It includes both completely

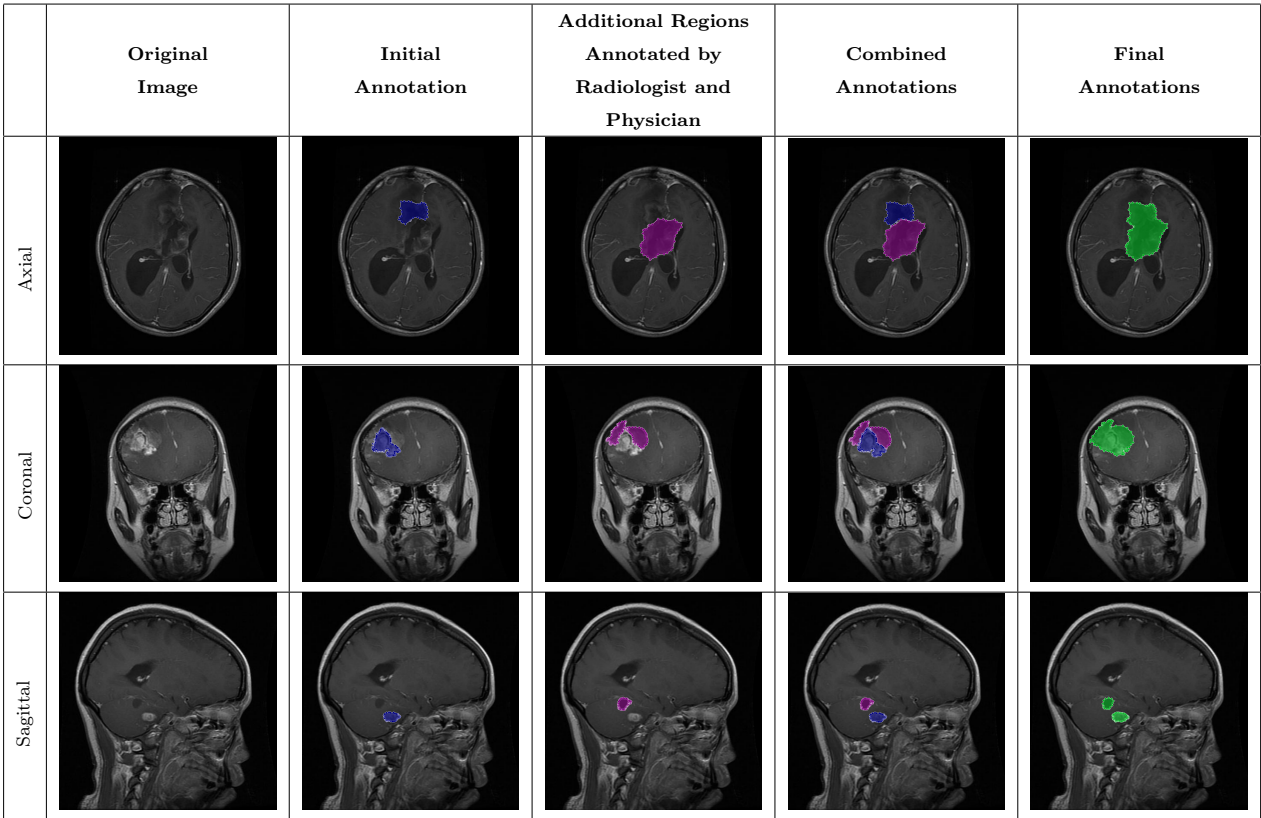|	Original Image	Initial Annotation	Additional Regions Annotated by Radiologist and Physician	Combined Annotations	Final Annotations
Axial					
Coronal					
Sagittal					

Fig. 7: Samples of partial-region underannotations. The purple area indicates regions that were initially marked as non-tumorous but were later identified by the radiologist and physician as tumorous.

healthy brains and scans with non-neoplastic, space-occupying lesions (e.g., abscesses, cysts). Images misclassified in the original datasets were corrected or removed as needed.

- **Consensus Reviews**: Annotation was carried out by a trained team and verified under the supervision of a certified radiologist and physician. Discrepancies were detected through visual comparison and overlap inspection in AnyLabeling and resolved collaboratively during review sessions. A quality assessment on a representative subset showed a mean Dice coefficient of 0.924 between initial and expert-verified masks. Approximately 4.8% of images required correction, after which full consensus and final approval were achieved for all BRISC annotations.

Visual Demonstrations of the Dataset

This section provides an in-depth exploration of the dataset through visual examples and analytical discussions, illustrating its structure, composition, and inherent challenges. These demonstrations aim to deepen understanding of the dataset's unique features while highlighting its potential applications in advanced segmentation and classification tasks.

Overview of Classes

The dataset encompasses four distinct classes: "Glioma", "Meningioma", "Pituitary" tumors, and "non-tumorous". As detailed in Section , each class presents unique characteristics and complexities. This subsection offers representative visual examples from each class, including raw MRI scans alongside their annotated tumor masks, emphasizing the diversity and precision of the dataset.

- **Glioma**: Gliomas are irregularly shaped and often infiltrate surrounding tissues, presenting significant challenges for precise boundary definition. These complexities require robust segmentation techniques to capture their variable morphology. As shown in Figure 1, gliomas exhibit irregular and diffuse growth patterns, which are highlighted through annotated tumor masks.
- **Meningioma**: Meningiomas arise from the meninges and are generally well-circumscribed and homoge-

neous, making them easier to segment. However, their location adjacent to critical structures such as dural sinuses and cranial nerves can complicate diagnostic tasks.An example of a meningioma and its segmentation mask is presented in Figure 2, illustrating the clarity of its boundaries.

- **Pituitary Tumors**: Located at the base of the brain near critical structures like the optic chiasm, pituitary tumors demand careful delineation to avoid diagnostic errors. As shown in Figure 3, the segmentation accurately captures the tumor's boundaries without encroaching on adjacent critical regions.
- **Non-tumorous**: This control class includes both *healthy brain scans without visible abnormalities* and *scans with non-neoplastic, space-occupying lesions* (e.g., cysts, abscesses, or vascular malformations). Incorporating such cases improves the dataset's robustness for both binary (tumorous vs. non-tumorous) and multi-class classification tasks. Figure 4 presents representative examples of healthy and non-tumorous lesion cases across different imaging planes.

Tumor Mask and Annotation Quality

Achieving accurate tumor segmentation required a meticulous process of iterative reviews and refinements, conducted in close collaboration with a physician and a radiologist. This collaborative effort was crucial in ensuring that the final annotations accurately reflected the true tumor boundaries, minimizing errors and improving the overall quality of the dataset.

In some cases, regions initially annotated as tumors were later identified by physician and radiologist as non-tumorous. These corrections were essential to avoid false positives that could mislead model training. An example of such a case is shown in Figure 5, where an area initially believed to be a tumor was excluded from the final annotation after expert review.

In other instances, certain areas that were mistakenly included as part of the tumor region were refined based on radiologist and physician feedback. These areas, though visually similar to tumor tissue, were determined to be non-tumorous upon closer examination. As illustrated in Figure 6, the removal of these incorrect segments resulted in more precise tumor masks and enhanced the reliability of the dataset.

Conversely, there were cases where genuine tumor regions had been overlooked during the initial annotation process. With input from the Physician and radiologist, these missing regions were added to the annotations, ensuring that the masks comprehensively captured all tumor areas. Figure 7 demonstrates an example of such an adjustment, where previously unannotated tumor segments were correctly incorporated into the final mask.

Challenges of non-tumorous Conditions

Non-tumorous conditions frequently mimic tumors in MRI scans, posing significant challenges not only for classification tasks but also for segmentation. This section visualizes examples of these conditions and compares them with actual tumors to highlight their distinctions.

Brain lesions, for instance, often resemble tumors both in shape and intensity. These similarities can lead to misclassification as well as erroneous segmentation of the lesion as a tumor. Cysts are another condition that can complicate both segmentation and classification. Typically fluid-filled and round, cysts may be mistaken for tumors during segmentation tasks due to their well-defined boundaries. Calcifications, which appear as hyperintense regions on MRI scans, can similarly lead to errors in both classification and segmentation. While their growth patterns differ from tumors, their intensity can cause segmentation models to incorrectly label them as tumorous regions.

These challenges underscore the critical importance of radiologist and physician expertise in ensuring accurate segmentation and classification of such conditions. The examples provided highlight the need for robust models capable of distinguishing these non-tumorous conditions from actual tumors in both classification and segmentation tasks.

Limitations and Intended Use

BRISC comprises only contrast-enhanced T1-weighted MRI images collected from multiple public datasets that lack comprehensive acquisition metadata such as scanner type, field strength, or sequence parameters. Consequently, detailed harmonization across hardware and protocol variations was not achievable. The dataset is intended primarily for research in algorithm benchmarking, model comparison, and methodological development for brain-tumour segmentation and classification tasks. It is not designed or validated for direct clinical diagnostic use. Users should be aware that models trained on BRISC may experience domain-shift when applied to non-contrast T1-weighted, T2-weighted, or institution-specific datasets, and additional data normalization or fine-tuning is recommended to mitigate such effects.

Data Records

The BRISC (BRain tumor Image Segmentation and Classification) dataset is available in Kaggle, Figshare, and Zenodo. The dataset release includes:

− Dataset images
− Manifest file (`manifest.csv`)
− JSON metadata (`manifest.json`)
− File checksums and per-file metadata

The public release follows the directory structure shown in Figure 8.

```
/brisc2025/
── classification_task/
    ── train/
        ── glioma/
        ── meningioma/
        ── no_tumor/
        ── pituitary/
    ── test/
        ── glioma/
        ── meningioma/
        ── no_tumor/
        ── pituitary/
── segmentation_task/
    ── train/
        ── images/
        ── masks/
    ── test/
        ── images/
        ── masks/
```
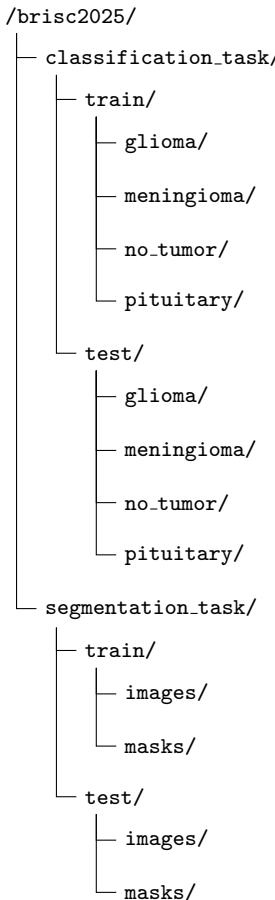
Fig. 8: Directory structure of the BRISC dataset.

File Naming Convention

Filenames follow this pattern:

`brisc2025_<split>_<index>_<tumor_code>_<plane_code>_<sequence>.<ext>`

Example: `brisc2025_test_00010_gl_ax_t1.jpg`

For segmentation pairs, images and masks share the same basename (image: `.jpg`, mask: `.png`).

Metadata Fields

Each image row in the manifest includes:

− `relative_path`, `filename`, `task`, `split`
− `index`, `tumor_code`, `tumor_label`
− `plane_code`, `plane_label` (ax=axial, co=coronal, sa=sagittal)
− `sequence` (e.g., t1=T1-weighted)
− Spatial dimensions (`width`, `height`)
− `file_size_bytes`, `sha256` checksum

Mask rows have `is_mask = True` and include `linked_image` pointing to the matched image.

BRISC is derived from Nickparvar "Brain Tumor MRI Dataset" [42], which aggregates:

− Cheng brain tumor dataset [13]
− SARTAJ [44]
− Br35H [45]

Selection and exclusion rules applied during curation are documented in the Methods section.

Data Overview

BRISC contains 2D single-slice T1-weighted brain MRI images stored as JPEG files, with corresponding pixel-wise segmentation masks stored as PNG files. The dataset is organized into two separate tasks:

1) **Classification task:** Balanced image-level classification dataset for four diagnostic classes: glioma, meningioma, pituitary tumor, and no_tumor. Contains 6,000 JPEG images (5,000 training, 1,000 test).

2) **Segmentation task:** Pixel-wise tumor annotation task. Contains 4,793 image files with exact paired masks.

Technical Validation

Establishing baseline performance is a critical step in evaluating any newly proposed dataset, as it sets a reference point for further research and model development [46]. To validate the effectiveness and versatility of the BRISC dataset, we conducted experimental evaluations on segmentation and classification tasks.

This section presents a comprehensive performance analysis of several standard baseline models. We report their performance metrics to establish clear benchmarks for the dataset. These results demonstrate the dataset's quality and utility for developing and testing new models in medical imaging.

Evaluation Metrics

Segmentation Metric

In this part, we detail the evaluation metrics employed to assess the performance of segmentation models on the BRISC dataset. These metrics provide comprehensive insights into model efficacy for these two distinct tasks.

Intersection over Union (IoU) Intersection over Union (IoU), also known as the Jaccard Index, is a fundamental metric for evaluating binary segmentation tasks. It quantifies the overlap between the predicted tumor regions and the ground truth, normalized by their union [47]. For binary segmentation, IoU is computed as shown in Equation 1.

$$\text{IoU} = \frac{\sum_{i=1}^{N} y_i \hat{y}_i}{\sum_{i=1}^{N} y_i + \sum_{i=1}^{N} \hat{y}_i - \sum_{i=1}^{N} y_i \hat{y}_i + \epsilon}, \quad (1)$$

where $y_i \in \{0,1\}$ denotes the ground truth label, $\hat{y}_i \in \{0,1\}$ represents the predicted label (after thresholding), and ϵ is a small constant added for numerical stability.

As shown in Equation 1, this formulation captures the pixel-wise overlap between the predicted and actual tumor regions and is particularly effective for evaluating segmentation quality, especially along object boundaries.

Classification Metrics

As commonly employed in the evaluation of multi-class classification models, metrics such as Accuracy, Precision, Recall, and F1-Score are widely utilized due to their effectiveness in assessing performance across diverse tasks [48, 49, 50]. These metrics are defined below to ensure a comprehensive understanding of their applicability to our dataset.

Accuracy Accuracy measures the overall correctness of predictions across all four classes. It is defined as:

$$\text{Accuracy} = \frac{\sum_{i=1}^{C} \text{Correct Predictions for Class } i}{\text{Total Samples}} \quad (2)$$

where C denotes the total number of classes, and "Correct Predictions for Class i" represents the samples correctly classified as class i.

Precision Precision quantifies the proportion of correctly predicted positive instances for each class. For class i, Precision is defined as:

$$\text{Precision}_i = \frac{\text{TP}_i}{\text{TP}_i + \text{FP}_i} \quad (3)$$

In multi-class classification, Precision is averaged using either macro-averaging or weighted-averaging:

$$\text{Macro Precision} = \frac{1}{C} \sum_{i=1}^{C} \text{Precision}_i \quad (4)$$

$$\text{Weighted Precision} = \frac{\sum_{i=1}^{C} w_i \cdot \text{Precision}_i}{\sum_{i=1}^{C} w_i} \quad (5)$$

where w_i represents the proportion of samples in class i.

Recall Recall, or Sensitivity, measures the proportion of actual positive instances correctly identified by the model. For class i, Recall is defined as:

$$\text{Recall}_i = \frac{\text{TP}_i}{\text{TP}_i + \text{FN}_i} \quad (6)$$

For multi-class classification, Recall is averaged similarly to Precision:

$$\text{Macro Recall} = \frac{1}{C} \sum_{i=1}^{C} \text{Recall}_i \quad (7)$$

$$\text{Weighted Recall} = \frac{\sum_{i=1}^{C} w_i \cdot \text{Recall}_i}{\sum_{i=1}^{C} w_i} \quad (8)$$

F1-Score The F1-Score is the harmonic mean of Precision and Recall. For class i, it is defined as:

$$\text{F1-Score}_i = 2 \cdot \frac{\text{Precision}_i \cdot \text{Recall}_i}{\text{Precision}_i + \text{Recall}_i} \quad (9)$$

For multi-class classification, F1-Score is averaged as follows:

$$\text{Macro F1-Score} = \frac{1}{C} \sum_{i=1}^{C} \text{F1-Score}_i \quad (10)$$

$$\text{Weighted F1-Score} = \frac{\sum_{i=1}^{C} w_i \cdot \text{F1-Score}_i}{\sum_{i=1}^{C} w_i} \qquad (11)$$

By calculating these metrics per class and aggregating them through macro- or weighted-averaging, we ensure a detailed evaluation of model performance, particularly in datasets with imbalanced class distributions.

Comparison

Segmentation results

To establish segmentation benchmarks for the dataset, we conducted a comparative study against a diverse set of brain tumor segmentation models, including traditional convolutional architectures, attention-enhanced methods, and transformer-based approaches. The baselines include UNet [51], UNet++ [52], LinkNet [54], MANet [53], DeepLabV3+ [55], PAN [56], EINet [57], EU-Net [58], DAD [59], and BASNet [60], as well as two recent transformer-enhanced models, SaberNet [61] and ABANet [62].

Each model was evaluated using the mean Intersection over Union (mIoU) metric for three tumor types: *Glioma*, *Meningioma*, and *Pituitary*. Furthermore, we report a *weighted mIoU*, which is calculated based on the proportion of samples belonging to each tumor type, providing a more representative performance indicator across the dataset.

As summarized in Table 3, the results establish a strong set of baselines. Transformer-based models, such as SaberNet, achieved the highest scores, with weighted mIoUs of 80.6% respectively. This suggests that architectures adept at capturing multi-scale contextual features perform well on this dataset. More traditional architectures like UNet provided a solid baseline with a weighted mIoU of 75.7%.

The reported weighted mIoU is calculated as a weighted average based on the number of samples in each tumor class to provide a more realistic assessment under dataset imbalance. Unlike simple arithmetic means, the weighted mean better reflects the overall segmentation performance in real-world clinical distributions.

It is important to emphasize that the primary goal of this work is to introduce and validate a new brain tumor segmentation dataset, which is designed to support the development of robust and generalizable medical segmentation models. These results serve as a foundational step, and future research is expected to build upon this dataset to explore a broader range of models, training protocols, and evaluation settings.

Classification Results

To evaluate the classification performance on our newly introduced brain tumor dataset, we conducted a comprehensive analysis of several baseline models for classifying brain tumor types: *Glioma*, *Meningioma*, *Pituitary*, and *non-tumorous*. The evaluated models include ResNet50, ResNet101, DenseNet121, DenseNet169, MobileNetV2, MobileNetV3, EfficientNetB0, EfficientNetB1, EfficientNetB2, Xception, VGG16, VGG19, and InceptionV3. Each model was trained and tested three times to ensure robust and reliable results, with performance reported as the mean and standard deviation of key metrics: Precision, Recall, F1-Score, and Accuracy.

The evaluation metrics were computed per class, alongside macro and weighted averages, to provide a comprehensive view of model performance across diverse tumor types. The macro average treats all classes equally, while the weighted average accounts for class imbalance by weighting each class's contribution based on the number of samples, offering a realistic assessment of performance in clinical scenarios where tumor type distributions may vary.

As presented in Table 4, the benchmarks show that high classification accuracy is achievable on this dataset. EfficientNetB0 performs strongly, with a weighted average F1-score of 0.9920 ± 0.0000 and an accuracy of 0.9920 ± 0.0000, achieving perfect recall (1.0000 ± 0.0000) for the *non-tumorous* class. EfficientNetB1 follows closely with a weighted F1-score of 0.9903 ± 0.0042, while ResNet50 and MobileNetV3 deliver competitive results (weighted F1-scores of 0.9820 ± 0.0080 and 0.9447 ± 0.0140, respectively).

In contrast, Xception exhibits the lowest performance, with a weighted F1-score of 0.1780 ± 0.0658, failing entirely on meningioma and pituitary (F1-score: 0.0000 ± 0.0000). Similarly, DenseNet121 and DenseNet169 show unstable performance, with high standard deviations, indicating limited generalizability. MobileNetV2 also struggles, particularly with meningioma (recall: 0.0120 ± 0.0180), likely due to insufficient model capacity.

The VGG variants (VGG16 and VGG19) achieve moderate performance, with weighted F1-scores of 0.9693 ± 0.0177 and 0.9630 ± 0.0044, respectively, while InceptionV3 shows inconsistent results (weighted F1-score: 0.6487 ± 0.4312), reflecting challenges in handling complex tumor morphology or class imbalances.

This evaluation underscores the strong performance of EfficientNet models, particularly EfficientNetB0, which combines high accuracy with remarkable stability across all tumor types. The results validate the utility of our dataset for developing reliable diagnostic tools,

Table 3: IoU (%) for Brain Tumor Segmentation Models on Different Tumor Types. Weighted mIoU is calculated as a weighted average based on the number of samples per tumor type: Glioma, Meningioma, Pituitary.

Model	mIoU Glioma	mIoU Meningioma	mIoU Pituitary	Weighted mIoU
UNet [51]	69.7	77.1	79.3	75.7
UNet++ [52]	71.7	74.2	79.7	75.3
MANet [53]	72.4	77.5	78.0	76.2
LinkNet [54]	71.7	74.8	79.0	75.3
DeepLabV3+ [55]	72.0	77.5	78.7	76.3
PAN [56]	72.0	74.5	80.7	75.9
EINet [57]	73.6	78.4	80.3	77.7
EU-Net [58]	71.7	76.1	78.3	75.6
DAD [59]	75.2	80.4	82.3	79.5
BASNet [60]	74.0	77.5	81.7	77.9
SaberNet [61]	74.0	82.4	84.3	80.6
ABANet [62]	72.4	80.4	84.7	79.5

while the stark performance differences across architectures emphasize the importance of model selection in medical imaging tasks, where precision and consistency are critical. This work establishes a robust benchmark for brain tumor classification and provides a foundation for future research to explore diverse models and training protocols using this dataset.

Data Availability

We introduce a new dataset, BRISC (Brain Tumor MRI Dataset for Segmentation and Classification), which is publicly available at:

1. Kaggle (`https://www.kaggle.com/datasets/briscdataset/brisc2025/`).
2. Figshare (`https://doi.org/10.6084/m9.figshare.30533120`).
3. Zenodo (`https://doi.org/10.5281/zenodo.17524350`)

Code Availability

The custom code developed for the baseline models are publicly available at the BRISC dataset repository on Kaggle: `https://www.kaggle.com/datasets/briscdataset/brisc2025/`.

Author Contributions

Amirreza Fateh wrote the original draft of the manuscript, supervised the research, and contributed to the methodology. Yasin Rezvani contributed to the dataset collection, curation, and methodology, and implemented the code. Sara Moayedi contributed to the dataset creation. Sadjad Rezvani contributed to the methodology and implemented the proposed method. Fatemeh Fateh, as the consulting physician, supervised the dataset design and labeling and contributed to writing the manuscript. Mansoor Fateh supervised the research, reviewed the manuscript, and contributed to the methodology. Vahid Abolghasemi reviewed the manuscript and supervised the work. All authors reviewed and approved the final manuscript.

Competing Interests

The authors declare no competing interests.

References

1. L.-K. Ge, P. Gao, D. Chang, J.-J. Nie, Y.-S. Wang, X.-N. Zuo, and G.-X. Wei, "An open data for imaging acute

Table 4: Per-Class and Average Classification Performance (%) for Brain Tumor Classification Models. Metrics are reported as mean ± standard deviation over three runs.

Model	Class	Precision	Recall	F1-Score	Accuracy
ResNet50	glioma	0.9868 ± 0.0098	0.9751 ± 0.0164	0.9808 ± 0.0103	-
	meningioma	0.9815 ± 0.0150	0.9673 ± 0.0226	0.9741 ± 0.0087	-
	no_tumor	0.9906 ± 0.0107	0.9952 ± 0.0083	0.9929 ± 0.0035	-
	pituitary	0.9756 ± 0.0285	0.9967 ± 0.0000	0.9859 ± 0.0146	-
	Macro Avg	0.9836 ± 0.0064	0.9836 ± 0.0077	0.9834 ± 0.0072	-
	Weighted Avg	0.9823 ± 0.0076	0.9820 ± 0.0080	0.9820 ± 0.0080	0.9820 ± 0.0080
ResNet101	glioma	0.9726 ± 0.0347	0.9869 ± 0.0082	0.9794 ± 0.0138	-
	meningioma	0.9879 ± 0.0081	0.9575 ± 0.0279	0.9722 ± 0.0106	-
	no_tumor	0.9883 ± 0.0107	0.9905 ± 0.0165	0.9893 ± 0.0037	-
	pituitary	0.9793 ± 0.0113	0.9956 ± 0.0020	0.9874 ± 0.0066	-
	Macro Avg	0.9820 ± 0.0074	0.9826 ± 0.0093	0.9821 ± 0.0086	-
	Weighted Avg	0.9815 ± 0.0085	0.9810 ± 0.0092	0.9810 ± 0.0092	0.9809 ± 0.0092
DenseNet121	glioma	0.4838 ± 0.4753	0.5879 ± 0.5095	0.5197 ± 0.4731	-
	meningioma	0.6640 ± 0.5751	0.2800 ± 0.4569	0.3178 ± 0.4966	-
	no_tumor	0.5324 ± 0.4095	0.6976 ± 0.4871	0.4721 ± 0.4204	-
	pituitary	0.4502 ± 0.4128	0.6422 ± 0.5574	0.5259 ± 0.4678	-
	Macro Avg	0.5326 ± 0.4550	0.5519 ± 0.3376	0.4589 ± 0.4310	-
	Weighted Avg	0.5356 ± 0.4650	0.5253 ± 0.3850	0.5253 ± 0.3850	0.4531 ± 0.4390
DenseNet169	glioma	0.9543 ± 0.0690	0.3543 ± 0.5356	0.3840 ± 0.5173	-
	meningioma	0.7522 ± 0.2090	0.8007 ± 0.2607	0.7560 ± 0.2021	-
	no_tumor	0.4841 ± 0.4507	0.9738 ± 0.0393	0.5754 ± 0.3763	-
	pituitary	0.3333 ± 0.5774	0.3322 ± 0.5754	0.3328 ± 0.5764	-
	Macro Avg	0.6310 ± 0.3116	0.6152 ± 0.3305	0.5121 ± 0.4160	-
	Weighted Avg	0.6404 ± 0.3020	0.5710 ± 0.3689	0.5710 ± 0.3689	0.5093 ± 0.4169
MobileNetV2	glioma	0.3026 ± 0.0558	0.8517 ± 0.1229	0.4418 ± 0.0494	-
	meningioma	0.6667 ± 0.5774	0.0120 ± 0.0180	0.0233 ± 0.0348	-
	no_tumor	0.5343 ± 0.3066	0.6548 ± 0.1750	0.5249 ± 0.0899	-
	pituitary	0.1412 ± 0.2445	0.0400 ± 0.0693	0.0623 ± 0.1080	-
	Macro Avg	0.4112 ± 0.2078	0.3896 ± 0.0345	0.2631 ± 0.0307	-
	Weighted Avg	0.3980 ± 0.2379	0.3237 ± 0.0264	0.3237 ± 0.0264	0.2115 ± 0.0366
MobileNetV3	glioma	0.8912 ± 0.0353	0.9777 ± 0.0082	0.9321 ± 0.0154	-
	meningioma	0.9755 ± 0.0050	0.8639 ± 0.0334	0.9160 ± 0.0175	-
	no_tumor	0.9445 ± 0.0308	1.0000 ± 0.0000	0.9713 ± 0.0165	-
	pituitary	0.9679 ± 0.0073	0.9733 ± 0.0208	0.9706 ± 0.0138	-
	Macro Avg	0.9448 ± 0.0148	0.9537 ± 0.0113	0.9475 ± 0.0140	-
	Weighted Avg	0.9475 ± 0.0123	0.9447 ± 0.0140	0.9447 ± 0.0140	0.9442 ± 0.0142
EfficientNetB0	glioma	0.9960 ± 0.0000	0.9882 ± 0.0000	0.9921 ± 0.0000	-
	meningioma	0.9934 ± 0.0000	0.9869 ± 0.0000	0.9902 ± 0.0000	-
	no_tumor	0.9929 ± 0.0000	1.0000 ± 0.0000	0.9964 ± 0.0000	-
	pituitary	0.9868 ± 0.0000	0.9967 ± 0.0000	0.9917 ± 0.0000	-
	Macro Avg	0.9923 ± 0.0000	0.9929 ± 0.0000	0.9926 ± 0.0000	-
	Weighted Avg	0.9920 ± 0.0000	0.9920 ± 0.0000	0.9920 ± 0.0000	0.9920 ± 0.0000
EfficientNetB1	glioma	0.9987 ± 0.0023	0.9921 ± 0.0000	0.9954 ± 0.0011	-
	meningioma	0.9933 ± 0.0001	0.9750 ± 0.0136	0.9840 ± 0.0070	-
	no_tumor	0.9976 ± 0.0041	1.0000 ± 0.0000	0.9988 ± 0.0021	-
	pituitary	0.9773 ± 0.0116	1.0000 ± 0.0000	0.9885 ± 0.0059	-
	Macro Avg	0.9918 ± 0.0036	0.9918 ± 0.0034	0.9917 ± 0.0036	-
	Weighted Avg	0.9905 ± 0.0040	0.9903 ± 0.0042	0.9903 ± 0.0042	0.9903 ± 0.0042
EfficientNetB2	glioma	0.9919 ± 0.0040	0.9712 ± 0.0164	0.9814 ± 0.0091	-
	meningioma	0.9699 ± 0.0128	0.9782 ± 0.0105	0.9740 ± 0.0084	-
	no_tumor	0.9906 ± 0.0107	1.0000 ± 0.0000	0.9953 ± 0.0054	-
	pituitary	0.9879 ± 0.0082	0.9922 ± 0.0077	0.9900 ± 0.0017	-
	Macro Avg	0.9851 ± 0.0054	0.9854 ± 0.0047	0.9852 ± 0.0051	-
	Weighted Avg	0.9838 ± 0.0049	0.9837 ± 0.0049	0.9837 ± 0.0049	0.9837 ± 0.0049
Xception	glioma	0.0847 ± 0.1466	0.3333 ± 0.5774	0.1350 ± 0.2339	-
	meningioma	0.0000 ± 0.0000	0.0000 ± 0.0000	0.0000 ± 0.0000	-
	no_tumor	0.0933 ± 0.0808	0.6667 ± 0.5774	0.1637 ± 0.1418	-
	pituitary	0.0000 ± 0.0000	0.0000 ± 0.0000	0.0000 ± 0.0000	-
	Macro Avg	0.0445 ± 0.0165	0.2500 ± 0.0000	0.0747 ± 0.0230	-
	Weighted Avg	0.0346 ± 0.0259	0.1780 ± 0.0658	0.1780 ± 0.0658	0.0572 ± 0.0395
VGG16	glioma	0.9803 ± 0.0150	0.9396 ± 0.0741	0.9582 ± 0.0335	-
	meningioma	0.9427 ± 0.0509	0.9684 ± 0.0019	0.9549 ± 0.0257	-
	no_tumor	0.9790 ± 0.0068	0.9976 ± 0.0041	0.9882 ± 0.0020	-
	pituitary	0.9867 ± 0.0099	0.9822 ± 0.0117	0.9844 ± 0.0051	-
	Macro Avg	0.9722 ± 0.0132	0.9720 ± 0.0172	0.9714 ± 0.0162	-
	Weighted Avg	0.9706 ± 0.0157	0.9693 ± 0.0177	0.9693 ± 0.0177	0.9692 ± 0.0178
VGG19	glioma	0.9484 ± 0.0351	0.9541 ± 0.0421	0.9502 ± 0.0081	-
	meningioma	0.9624 ± 0.0130	0.9434 ± 0.0068	0.9527 ± 0.0030	-
	no_tumor	0.9725 ± 0.0231	0.9976 ± 0.0041	0.9848 ± 0.0111	-
	pituitary	0.9744 ± 0.0287	0.9745 ± 0.0267	0.9739 ± 0.0039	-
	Macro Avg	0.9645 ± 0.0061	0.9674 ± 0.0041	0.9654 ± 0.0047	-
	Weighted Avg	0.9639 ± 0.0039	0.9630 ± 0.0044	0.9630 ± 0.0044	0.9629 ± 0.0044
InceptionV3	glioma	0.6564 ± 0.5686	0.5315 ± 0.4983	0.5778 ± 0.5128	-
	meningioma	0.8972 ± 0.1694	0.6645 ± 0.5132	0.6401 ± 0.4458	-
	no_tumor	0.5887 ± 0.4180	0.9905 ± 0.0165	0.6719 ± 0.3794	-
	pituitary	0.6629 ± 0.5741	0.5722 ± 0.5136	0.6104 ± 0.5343	-
	Macro Avg	0.7013 ± 0.3670	0.6897 ± 0.3750	0.6250 ± 0.4676	-
	Weighted Avg	0.7225 ± 0.3490	0.6487 ± 0.4312	0.6487 ± 0.4312	0.6198 ± 0.4797

aerobic exercise effects on brain and mind in emerging adulthood," *Scientific Data*, vol. 11, no. 1, p. 1422, 2024.

2. M. Usman Akbar, M. Larsson, I. Blystad, and A. Eklund, "Brain tumor segmentation using synthetic mr images-a comparison of gans and diffusion models," *Scientific Data*, vol. 11, no. 1, p. 259, 2024.

3. Z. Sun, J. Huang, X. Ma, J. Liang, C. Sun, L. Hu, H. He, and G. Yu, "A low-field mri dataset for spatiotemporal analysis of developing brain," *Scientific Data*, vol. 12, no. 1, p. 109, 2025.

4. Q. Zhu, S. Li, Z. Cao, Y. Shen, H. Xu, G. Xu, H. Li, Z. Cui, K. Zhu, Z. Zhao *et al.*, "7 tesla multimodal mri dataset of ex-vivo human brain," *Scientific Data*, vol. 12, no. 1, p. 845, 2025.

5. Z. Gong, T. Xu, N. Peng, X. Cheng, C. Niu, B. Wiestler, F. Hong, and H. B. Li, "A multi-center, multi-parametric mri dataset of primary and secondary brain tumors," *Scientific Data*, vol. 11, no. 1, p. 789, 2024.

6. S. Dorosti, T. Landry, K. Brewer, A. Forbes, C. Davis, and J. Brown, "High-resolution ultrasound data for ai-based segmentation in mouse brain tumor," *Scientific Data*, vol. 12, no. 1, p. 1322, 2025.

7. C. Li, D. Yang, S. Yao, S. Wang, Y. Wu, L. Zhang, Q. Li, K. I. K. Cho, J. Seitz-Holland, L. Ning *et al.*, "Ddevenet: Evidence-based ensemble learning for uncertainty-aware brain parcellation using diffusion mri," *Computerized Medical Imaging and Graphics*, vol. 120, p. 102489, 2025.

8. S. Rezvani, M. Fateh, Y. Jalali, and A. Fateh, "Fusionlungnet: Multi-scale fusion convolution with refinement network for lung ct image segmentation," *Biomedical Signal Processing and Control*, vol. 107, p. 107858, 2025.

9. Q. Zhang, Y. Hang, J. Qiu, and H. Chen, "Application of u-net network utilizing multiattention gate for mri segmentation of brain tumors," *Journal of Computer Assisted Tomography*, vol. 48, no. 6, pp. 991–997, 2024.

10. F. Askari, A. Fateh, and M. R. Mohammadi, "Enhancing few-shot image classification through learnable multiscale embedding and attention mechanisms," *Neural Networks*, vol. 187, p. 107339, 2025.

11. A. Fateh, M. R. Mohammadi, and M. R. Jahed-Motlagh, "Msdnet: Multi-scale decoder for few-shot semantic segmentation via transformer-guided prototyping," *Image and Vision Computing*, vol. 162, p. 105672, 2025. [Online]. Available: https://www.sciencedirect.com/science/article/pii/S0262885625002604

12. B. H. Menze, A. Jakab, S. Bauer, J. Kalpathy-Cramer, K. Farahani, J. Kirby, Y. Burren, N. Porz, J. Slotboom, R. Wiest *et al.*, "The multimodal brain tumor image segmentation benchmark (brats)," *IEEE transactions on medical imaging*, vol. 34, no. 10, pp. 1993–2024, 2014.

13. J. Cheng, "brain tumor dataset," 4 2017. [Online]. Available: https://figshare.com/articles/dataset/brain_tumor_dataset/1512427

14. M. Ghaffari, A. Sowmya, and R. Oliver, "Automated brain tumor segmentation using multimodal brain scans: a survey based on models submitted to the brats 2012–2018 challenges," *IEEE reviews in biomedical engineering*, vol. 13, pp. 156–168, 2019.

15. D. LaBella, U. Baid, O. Khanna, S. McBurney-Lin, R. McLean, P. Nedelec, A. Rashid, N. H. Tahon, T. Altes, R. Bhalerao *et al.*, "Analysis of the brats 2023 intracranial meningioma segmentation challenge," *arXiv preprint arXiv:2405.09787*, 2024.

16. S. G. De Benedictis, G. Gargano, and G. Settembre, "Enhanced mri brain tumor detection and classification via

17. topological data analysis and low-rank tensor decomposition," *Journal of Computational Mathematics and Data Science*, vol. 13, p. 100103, 2024.

17. S. Sarkar, H. Singh, and J. Chawla, "Evolution of lung tumor segmentation: Comprehensive analysis," in *2024 International Conference on Advances in Computing, Communication and Applied Informatics (ACCAI)*. IEEE, 2024, pp. 1–7.

18. H. R. Khajeha, M. Fateh, V. Abolghasemi, A. R. Fateh, M. H. Emamian, H. Hashemi, and A. Fotouhi, "Advancing glaucoma diagnosis through multi-scale feature extraction and cross-attention mechanisms in optical coherence tomography images," *Engineering Reports*, vol. 7, no. 4, p. e70110, 2025.

19. M. S. Fakhima, M. Fateh, A. Fateh, and Y. Jalalia, "Dacovsgnet: Double attentional network for covid severity grading," *International Journal of Engineering, Transactions A: Basics*, vol. 38, no. 07, pp. 1568–82, 2025.

20. S. Rezvani, F. S. Siahkar, Y. Rezvani, A. A. Gharahbagh, and V. Abolghasemi, "Single image denoising via a new lightweight learning-based model," *IEEE Access*, 2024.

21. K. Aldape, K. M. Brindle, L. Chesler, R. Chopra, A. Gajjar, M. R. Gilbert, N. Gottardo, D. H. Gutmann, D. Hargrave, E. C. Holland *et al.*, "Challenges to curing primary brain tumours," *Nature reviews Clinical oncology*, vol. 16, no. 8, pp. 509–520, 2019.

22. E. M. Senan, M. E. Jadhav, T. H. Rassem, A. S. Aljaloud, B. A. Mohammed, and Z. G. Al-Mekhlafi, "Early diagnosis of brain tumour mri images using hybrid techniques between deep and machine learning," *Computational and Mathematical Methods in Medicine*, vol. 2022, no. 1, p. 8330833, 2022.

23. S. Lapointe, A. Perry, and N. A. Butowski, "Primary brain tumours in adults," *The Lancet*, vol. 392, no. 10145, pp. 432–446, 2018.

24. S. Sunaert, "Presurgical planning for tumor resectioning," *Journal of Magnetic Resonance Imaging: An Official Journal of the International Society for Magnetic Resonance in Medicine*, vol. 23, no. 6, pp. 887–905, 2006.

25. A. Fateh, M. Rezvani, A. Tajary, and M. Fateh, "Providing a voting-based method for combining deep neural network outputs to layout analysis of printed documents," *Journal of Machine Vision and Image Processing*, vol. 9, no. 1, pp. 47–64, 2022.

26. A. Mehndiratta and F. L. Giesel, *Brain tumour imaging*. INTECH Open Access Publisher, 2011.

27. A. Perry and P. Wesseling, "Histologic classification of gliomas," *Handbook of clinical neurology*, vol. 134, pp. 71–95, 2016.

28. K. R. Jessen, "Glial cells," *The international journal of biochemistry & cell biology*, vol. 36, no. 10, pp. 1861–1867, 2004.

29. A.-R. Fathi and U. Roelcke, "Meningioma," *Current neurology and neuroscience reports*, vol. 13, pp. 1–8, 2013.

30. K. Dasgupta and J. Jeong, "Developmental biology of the meninges," *genesis*, vol. 57, no. 5, p. e23288, 2019.

31. C. Marosi, M. Hassler, K. Roessler, M. Reni, M. Sant, E. Mazza, and C. Vecht, "Meningioma," *Critical reviews in oncology/hematology*, vol. 67, no. 2, pp. 153–171, 2008.

32. P.-F. Yan, L. Yan, T.-T. Hu, D.-D. Xiao, Z. Zhang, H.-Y. Zhao, and J. Feng, "The potential value of preoperative mri texture and shape analysis in grading meningiomas: a preliminary investigation," *Translational oncology*, vol. 10, no. 4, pp. 570–577, 2017.

33. R. E. Bancalari, L. C. Gregory, M. J. McCabe, and M. T. Dattani, "Pituitary gland development: an update," *Endocr Dev*, vol. 23, no. 1, 2012.

34. S. L. Asa and S. Ezzat, "The pathogenesis of pituitary tumours," *Nature Reviews Cancer*, vol. 2, no. 11, pp. 836–849, 2002.

35. G. Raverot, M. D. Ilie, H. Lasolle, V. Amodru, J. Trouillas, F. Castinetti, and T. Brue, "Aggressive pituitary tumours and pituitary carcinomas," *Nature Reviews Endocrinology*, vol. 17, no. 11, pp. 671–684, 2021.

36. A. Kelly, "Neurological therapeutics: Principles andpractice, secondedition," 2008.

37. A. Reang, "Clinico-radiologic profile of intracranial space occupying lesion imaged with mri and spectroscopy in a tertiary care centre," *International Journal of Life Sciences, Biotechnology and Pharma Research*, vol. 14, 2025.

38. Kenhub, "Anatomical terminology: Planes, directions & regions," 2025, accessed: 2025-05-31. [Online]. Available: https://www.kenhub.com/en/library/anatomy/anatomical-terminology

39. C. Westbrook and J. Talbot, *MRI in Practice*. John Wiley & Sons, 2018.

40. A. M. Omuro, C. C. Leite, K. Mokhtari, and J.-Y. Delattre, "Pitfalls in the diagnosis of brain tumours," *The Lancet Neurology*, vol. 5, no. 11, pp. 937–948, 2006.

41. P.-F. Yan, L. Yan, Z. Zhang, A. Salim, L. Wang, T.-T. Hu, and H.-Y. Zhao, "Accuracy of conventional mri for preoperative diagnosis of intracranial tumors: A retrospective cohort study of 762 cases," *International Journal of Surgery*, vol. 36, pp. 109–117, 2016.

42. M. Nickparvar, "Brain tumor mri dataset," Kaggle Dataset, 2021, https://www.kaggle.com/datasets/masoudnickparvar/brain-tumor-mri-dataset.

43. V. Nguyen, "Anylabeling-effortless data labeling with ai support," 2024.

44. S. Bhuvaji, A. Kadam, P. Bhumkar, and S. Dedge, "Brain tumor classification (mri)," Kaggle Dataset, 2021, https://www.kaggle.com/datasets/sartajbhuvaji/brain-tumor-classification-mri.

45. A. Hamada, "Br35h :: Brain tumor detection 2020," Kaggle Dataset, 2020, https://www.kaggle.com/datasets/ahmedhamada0/brain-tumor-detection?select=no.

46. J. Cheng, B. Fu, J. Ye, G. Wang, T. Li, H. Wang, R. Li, H. Yao, J. Chen, J. Li *et al.*, "Interactive medical image segmentation: A benchmark dataset and baseline," *arXiv preprint arXiv:2411.12814*, 2024.

47. H. Rezatofighi, N. Tsoi, J. Gwak, A. Sadeghian, I. Reid, and S. Savarese, "Generalized intersection over union: A metric and a loss for bounding box regression," in *Proceedings of the IEEE/CVF conference on computer vision and pattern recognition*, 2019, pp. 658–666.

48. I. Goodfellow, "Deep learning," 2016.

49. K. He, X. Zhang, S. Ren, and J. Sun, "Deep residual learning for image recognition," in *Proceedings of the IEEE conference on computer vision and pattern recognition*, 2016, pp. 770–778.

50. A. Dosovitskiy, "An image is worth 16x16 words: Transformers for image recognition at scale," *arXiv preprint arXiv:2010.11929*, 2020.

51. O. Ronneberger, P. Fischer, and T. Brox, "U-net: Convolutional networks for biomedical image segmentation," in *Medical image computing and computer-assisted intervention–MICCAI 2015: 18th international conference, Munich, Germany, October 5-9, 2015, proceedings, part III 18*. Springer, 2015, pp. 234–241.

52. Z. Zhou, M. M. Rahman Siddiquee, N. Tajbakhsh, and J. Liang, "Unet++: A nested u-net architecture for medical image segmentation," in *Deep learning in medical image analysis and multimodal learning for clinical decision support: 4th international workshop, DLMIA 2018, and 8th international workshop, ML-CDS 2018, held in conjunction with MICCAI 2018, Granada, Spain, September 20, 2018, proceedings 4*. Springer, 2018, pp. 3–11.

53. T. Fan, G. Wang, Y. Li, and H. Wang, "Ma-net: A multiscale attention network for liver and tumor segmentation," *IEEE Access*, vol. 8, pp. 179 656–179 665, 2020.

54. A. Chaurasia and E. Culurciello, "Linknet: Exploiting encoder representations for efficient semantic segmentation," in *2017 IEEE visual communications and image processing (VCIP)*. IEEE, 2017, pp. 1–4.

55. L.-C. Chen, Y. Zhu, G. Papandreou, F. Schroff, and H. Adam, "Encoder-decoder with atrous separable convolution for semantic image segmentation," in *Proceedings of the European conference on computer vision (ECCV)*, 2018, pp. 801–818.

56. H. Li, P. Xiong, J. An, and L. Wang, "Pyramid attention network for semantic segmentation," *arXiv preprint arXiv:1805.10180*, 2018.

57. C. Li and G. Jiao, "Einet: camouflaged object detection with pyramid vision transformer," *Journal of Electronic Imaging*, vol. 31, no. 5, pp. 053 002–053 002, 2022.

58. K. Patel, A. M. Bur, and G. Wang, "Enhanced u-net: A feature enhancement network for polyp segmentation," in *2021 18th conference on robots and vision (CRV)*. IEEE, 2021, pp. 181–188.

59. J. Li, W. He, and H. Zhang, "Towards complex backgrounds: A unified difference-aware decoder for binary segmentation," *arXiv preprint arXiv:2210.15156*, 2022.

60. X. Qin, D.-P. Fan, C. Huang, C. Diagne, Z. Zhang, A. C. Sant'Anna, A. Suarez, M. Jagersand, and L. Shao, "Boundary-aware segmentation network for mobile and web applications," *arXiv preprint arXiv:2101.04704*, 2021.

61. A. Saber, P. Parhami, A. Siahkarzadeh, M. Fateh, and A. Fateh, "Efficient and accurate pneumonia detection using a novel multi-scale transformer approach," *arXiv preprint arXiv:2408.04290*, 2024.

62. S. Rezvani, M. Fateh, and H. Khosravi, "Abanet: Attention boundary-aware network for image segmentation," *Expert Systems*, vol. 41, no. 9, p. e13625, 2024.